Optical and Quantum Communications

RLE Group
Optical and Quantum Communications Group

Academic and Research Staff
Professor Jeffrey H. Shapiro, Dr. Franco N. C. Wong, Dr. Lorenzo Maccone, Dr. Ranjith Nair, Dr. Raúl García-Patrón, Dr. Julien Le Gouët, Dr. Maria Tengner, Dr. Mankei Tsang, Dr. Valentina Schettini

Graduate Students
Christopher G. Blake, Fabrizio Guerrieri, Nicholas D. Hardy, Bhaskar Mookerji, Veronika Stelmakh, Dheera Venkatraman, Wenbang Xu, Tian Zhong

The central theme of our programs has been to advance the understanding of optical and quantum communication, radar, and sensing systems. Broadly speaking, this has entailed: (1) developing system-analytic models for important propagation, detection, and communication scenarios; (2) using these models to derive the fundamental limits on system performance; and (3) identifying, and establishing through experimentation the feasibility of, techniques and devices which can be used to approach these performance limits.

Sponsors
Air Force Research Laboratory Contract FA8750-09-C-0194
Army Research Office – Grant W911NF-05-1-019
NIST - Grant 70NANB7H6186
Office of Naval Research - Contract N00014-08-1-1247
Office of Naval Research - Contract N66001-09-1-2028
U.S. Department of Interior Contract NBCHC00671
W. M. Keck Foundation Center for Extreme Quantum Information Theory
National Science Foundation Grant DGE-0801525

We are embarked on research in the area of quantum information technology whose goal is to enable the quantum-mechanical information transmission, storage, and processing needed for future applications in quantum computing and quantum communication. Our theoretical work is currently focused on the fundamental limits on classical information transmission that are due to the quantum noise of bosonic channels, and on the use of quantum resources in precision measurement and imaging applications. Our main experimental work is focused on generation and application of entanglement sources with high brightness and wavelength tunability. In addition, we are interested in novel entanglement sources and their applications in quantum logic gates, enhanced quantum measurements, quantum imaging, quantum protocols for entanglement distillation, and quantum cryptography.

<u>Fiber-Optic Distribution of Polarization Entangled Photons</u> The capability to efficiently generate and distribute high-quality entangled photons is key to many applications of photonic quantum information processing, such as quantum key distribution and linear optics quantum computing. In recent years most entanglement sources have been based on spontaneous parametric downconversion (SPDC) in quasi-phase-matched bulk nonlinear crystals such as periodically-poled potassium titanyl phosphate (PPKTP) or periodically-poled lithium niobate (PPLN) [1]. We have recently reported a photon-pair source using a PPKTP waveguide that is significantly more efficient than bulk crystal sources [2]. During the past year, in collaboration with Professor Karl Berggren, we have used the PPKTP waveguide source to generate high quality polarization-entangled photons and distribute them over a 200-meter fiber-optic link [3]. The polarization entanglement quality was found to be stable for ~30 min. without active control of the fiber-optic

link, suggesting potential applications in short-distance fiber-optic distribution of polarization entanglement, for instance, in networking between photonic and atomic qubit systems.

SPDC generation efficiency in bulk crystals is typically in the range of 10^{-12} to 10^{-8}, depending on the type of crystal, the crystal length, collection angle and bandwidth. Nonlinear waveguides, on the other hand, have been shown to have a significantly higher SPDC efficiency [2,4]. In our waveguide work [2] we show theoretically that the enhancement originates from the transverse index profile of a nonlinear crystal waveguide that imposes an effective transverse momentum on the phase-matching conditions. The added transverse momentum leads to a broader transverse spatial bandwidth of the signal and idler outputs, which in turn explains the much higher spectral brightness of a waveguide SPDC source compared with a bulk-crystal SPDC source.

Figure 1 shows the schematic of our experimental setup for demonstrating polarization entanglement distribution over a 200-m fiber-optic link between adjacent MIT Buildings 36 and 38 [3]. The 16-mm long fiber-coupled Rb-indiffused PPKTP waveguide was fabricated by AdvR, Inc. for type-II phase matching with orthogonally-polarized degenerate outputs at 1316 nm. The signal and idler outputs were separated by a polarizing beam splitter (PBS) and recombined at a 50-50 non-polarizing beam splitter (NPBS) that postselectively generated a pair of polarization-entangled photons in separate single-mode optical fibers. The optical link consisted of two 200-m single-mode (SMF-28) optical fibers between the source laboratory in Building 36 and the Berggren laboratory housing a superconducting nanowire single-photon detector (SNSPD) [5] located in Building 38. See the chapter Quantum Nanostructures and Nanofabrication in this Report for details of the design, fabrication, and characteristics of SNSPDs. The two entangled photons were polarization analyzed at the remote location before coincidence detection using a single SNSPD with a time-multiplexing scheme.

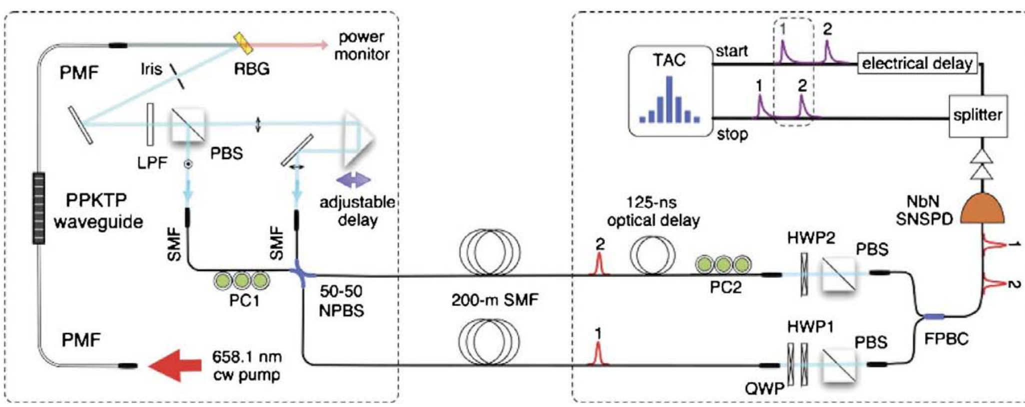

Figure 1. Schematic of experimental setup for polarization entanglement generation in a PPKTP waveguide, distribution over a 200-m fiber-optic link, and polarization analysis followed by time-multiplexed two-photon coincidence detection with a single SNSPD at the remote location.

Figure 2 shows the two-photon quantum-interference measurements of the distributed polarization-entangled photons in the horizontal-vertical (*H*-*V*) and antidiagonal-diagonal (*A*-*D*) polarization bases. To avoid degradation due to multiple-pair events, the measurements were made at a pump power of only 25 μW. We obtained visibilities of 98.2% and 97.2% in the *H*-*V* and *A*-*D* bases, respectively, without subtraction of accidental coincidences. Compared with a separate quantum-interference measurement with polarization analysis before the photons were sent through the fiber link (with visibilities of 98.3% and 97.2%), the fiber-optic transmission of the entangled photons showed no visibility degradation over the 200-m fiber link.

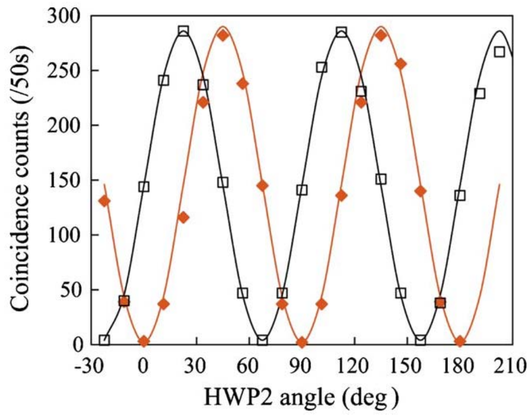

Figure 2. Two-photon quantum interference of distributed polarization-entangled photons in the *H-V* basis (filled diamonds) and the *A-D* basis (open squares) at 25 μW pump power without subtraction of accidentals [3]. Solid curves are sinusoidal fits.

Polarization entanglement may degrade in fiber propagation owing to depolarization mechanisms such as temperature fluctuation and mechanical vibration. We investigated the quality of the distributed entanglement over time by repeatedly measuring the two-photon quantum-interference visibility in both the *H-V* and *A-D* bases over a duration of 150 min. Figure 3 shows the results in which the time origin refers to the starting point when the polarizations were set correctly and the system was left unattended thereafter. We found that the visibility remained high at greater than 97% for ~30 min. without active polarization control [3]. This suggests that high-quality polarization entanglement can be easily distributed over short distances, such as between laboratories on campus, for an extended period of time if simple active polarization control is implemented. The compact waveguide source with its high SPDC generation efficiency and high entanglement quality will play an increasing role in future photonic sources for quantum information science such as linear-optics quantum computing.

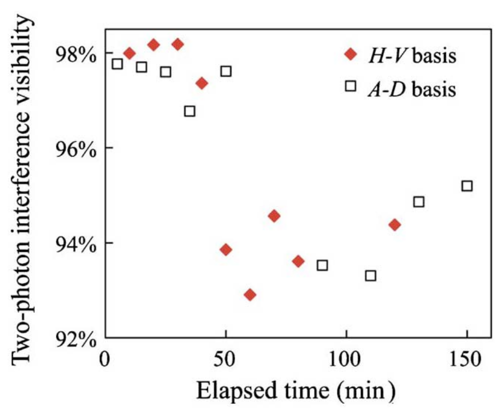

Figure 3. Time evolution of two-photon quantum-interference visibility in the *H-V* (filled diamonds) and *A-D* (open squares) bases for distributed polarization entanglement over two 200-m unattended fibers.

<u>Imaging with Phase-Sensitive Light</u> We have been exploring the use of phase-sensitive light in a variety of imaging scenarios in both quantum and quantum-mimetic imaging scenarios. A pair of Gaussian-state light beams that possess a phase-sensitive cross correlation can be produced by continuous-wave (cw) spontaneous parametric downconversion (SPDC) with vacuum-state signal and idler inputs [1,6,7]. The low-flux limit of cw SPDC can then be approximated by a vacuum

state plus a frequency-entangled biphoton. Many quantum imaging scenarios have been characterized — both theoretically and experimentally — in terms of postselected biphoton detection, e.g., quantum optical coherence tomography [8,9], ghost imaging [10], and two-photon imaging [11,12]. The primary objective of our work has been to clearly delineate the boundary between classical and quantum behavior in these and other imaging scenarios and to use this understanding to develop new, and more robust imaging schemes that offer advantages over classical techniques. What follows is a brief summary of our ongoing work in ghost imaging.

Ghost imaging is the acquisition of the transmittance pattern of an object through intensity correlation measurements, and it has been demonstrated with both thermal (classical) light and biphoton (quantum) light [10,13-15]. We have used our coherence theory [16] for Gaussian-state sources — which encompasses both thermal light and biphoton-state light as special cases — to show that almost all the characteristics of quantum ghost imaging are due to the phase-sensitive cross correlation between the signal and reference beams [17,18]. The particular ghost-imaging setup that we considered is shown in Fig. 4. For this arrangement we showed that thermal light, classical phase-sensitive light, and quantum phase-sensitive light all yield ghost images in both near-field and far-field operation. The same image inversion that has been seen in the quantum phase-sensitive light case, but not the thermal light case, turns out to be present for ghost imaging with classical phase-sensitive light. If the ghost-imager's source fields are constrained to have specific phase-insensitive auto-correlations, then quantum light offers a spatial resolution advantage in the source's near field and improved field-of-view in the far field. The principal advantage of quantum ghost imaging, however, comes from the near-absence of any background term in the ghost image. We have reported a comprehensive analysis of the signal-to-noise ratio (SNR) behavior obtained with thermal light, classical phase-sensitive light, and quantum phase-sensitive light [19], as well as conceiving two new configurations for ghost imaging [20].

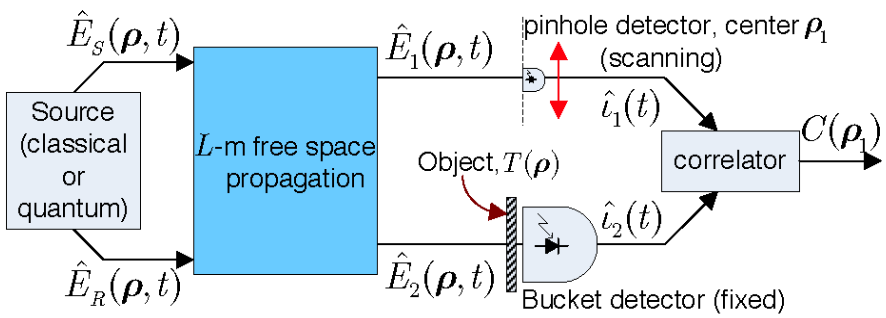

Figure 4. Schematic for transmissive ghost imaging. The signal and reference are broadband light beams with either a phase-insensitive or phase-sensitive cross correlation. After propagation over an *L*-m-long free space path, the signal beam illuminates a scanning pinhole detector and the reference illuminates an object transmittance mask followed by a large-area (bucket) detector. Cross correlating the resulting (shot-noise limited) photocurrents as the pinhole detector is scanned yields the ghost image.

Our SNR analysis permits, for the first time, a meaningful comparison between quantum-state and thermal-state ghost imaging performance with respect to their image acquisition time. i.e., the integration time required to achieve a desired SNR value for the image. For the important case of far-field broadband entangled-state imaging versus far-field narrowband thermal-state imaging we find that neither one enjoys a universal advantage, viz., depending on the parameter values involved either the quantum or the classical-state system may have the shorter image acquisition time [19].

The correlation-based theory we have developed for ghost imaging has recently led us to conceive two novel configurations for ghost imaging: spatial-light modulator (SLM) ghost imaging and computational ghost imaging [20], as shown in Figs. 5 and 6, respectively. In SLM ghost imaging we transmit a cw laser beam through a spatial light modulator that imposes an independent deterministic phase shift on each pixel such that the output field mimics a source of low spatial coherence. The rest of the setup is the same as a thermal-light lensless ghost imager. Our analysis shows that this arrangement yields a far-field ghost image with essentially the same field-of-view and spatial resolution characteristics as found previously for thermal-state ghost imaging. In particular, the field of view is inversely proportional to the effective coherence length at the output of the SLM and the spatial resolution in inversely proportional to the beam size at the output of the SLM.

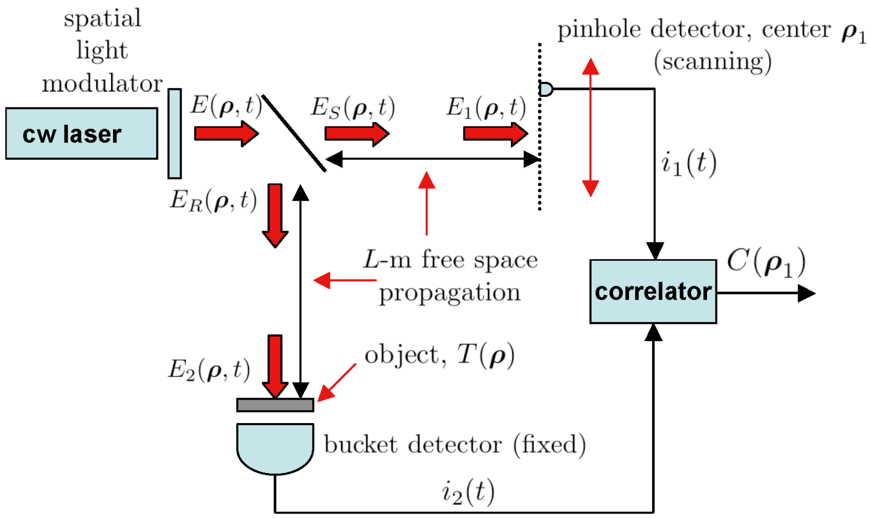

Figure 5. Configuration for spatial light modulator ghost imaging. The output from a cw laser is passed through a spatial light modulator driven by deterministic waveforms that impose different phase shifts on each pixel such that the output field mimics a source of low spatial coherence. The remainder of the setup is the same as a thermal-light lensless ghost imager.

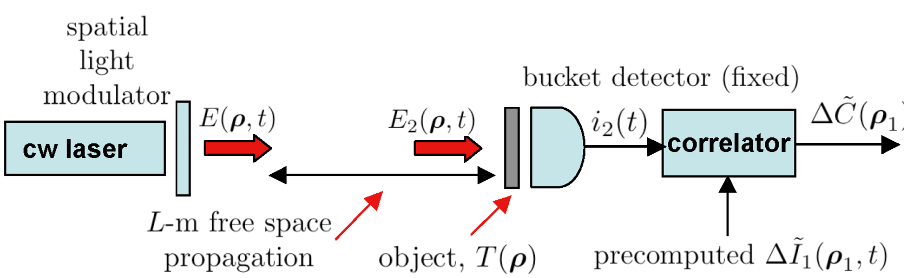

Figure 6. Configuration for computational ghost imaging. The output from a cw laser is passed through a spatial light modulator driven by deterministic waveforms that impose different phase shifts on each pixel such that the output field mimics a source of low spatial coherence. The remainder of the setup is the same as a thermal-light lensless ghost imager except that the reference path is derived by computing the free-space diffraction integral of the output field obtained from the spatial light modulator.

The transition from SLM ghost imaging to computational ghost imaging arises from the realization that we can precompute the reference field arriving at the high-resolution detector, in this case, because it is due to free-space diffraction of the deterministic light field obtained from passing the cw laser beam through the spatial light modulator. Aside from eliminating the need for a high spatial-resolution reference-path detector, computational ghost imaging allows the reference field to be precomputed for a range of path lengths, hence by correlating the bucket detector's output with these precomputed quantities permits range sectioning to be performed using a single data collection, something that is not possible in conventional ghost imaging. In this regard it is worth noting that proof-of-principle experiments have already demonstrated the basic features we predicted for computational ghost imaging [21].

During the past year we have begun a theoretical study of reflective ghost imaging, which, as shown in Fig. 7, is the configuration that is needed for standoff sensing. Unlike the transmissive case, ghost imaging done in reflection must cope with the effects of rough-surface scattering from the target being imaged. So far we have shown [22] that the target-induced speckle created by this rough-surface scattering does not affect the spatial resolution or image contrast behavior of the ghost image formed with pseudothermal (classical, phase-insensitive) light, but it does set an upper limit to the SNR that is not present in the transmissive case.

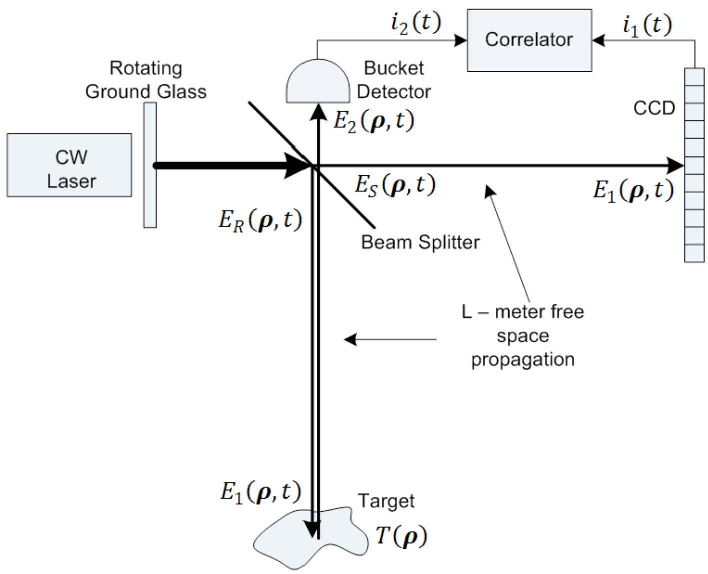

Figure 7. Configuration for pseudothermal reflective ghost imaging. The output from a cw laser is passed through a rotating ground-glass diffuser and then split into identical signal and reference beams. The signal is collected by a CCD camera after *L*-m-long free-space diffraction. The reference illuminates a rough-surfaced target at range L and the reflected light is measured by a single-pixel (bucket) detector. The ghost image is formed by cross correlating the photocurrents from the CCD array and the bucket detector.

During the past year we have begun an experimental program to explore ghost imaging. Figure 8 shows the experimental configuration for SLM ghost imaging using two SLMs that allows both phase-sensitive and phase-insensitive cross correlation to be implemented. The input beam is a cw laser at 795 nm in a single spatial mode that is split into a reference beam and a signal beam. The two beams undergo correlated phase-pattern modification imposed by the two spatial light modulators. For phase-insensitive (-sensitive) cross correlation, the two SLMs have equal-phase (anti-phase) patterns that are computer generated and updated in real time at a rate of 2 Hz. The random phase patterns create random speckle patterns for the signal and reference beams in the far field. The object is placed in the signal path and its transmitted light is collected by a single-pixel bucket detector. A CCD camera is placed in the reference beam path at a distance equal to the SLM-to-object distance. Intensity correlations between the outputs of the bucket detector and the CCD camera pixels are averaged and processed to generate the ghost image. The average light level gives rise to a featureless background that is subtracted to improve the image contrast.

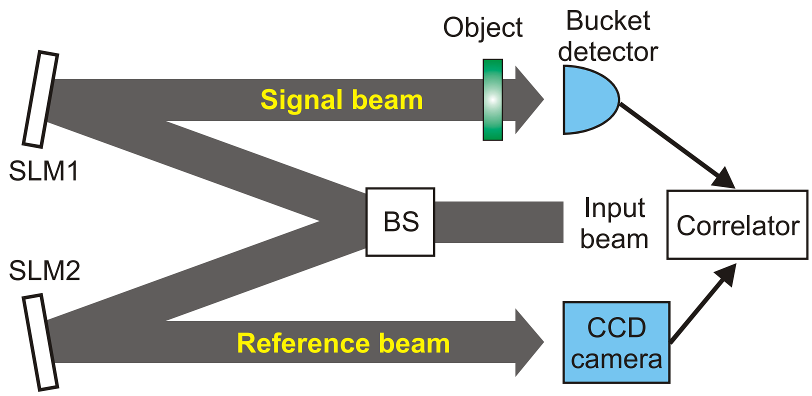

Figure 8. Schematic of experimental setup for spatial-light modulator (SLM) ghost imaging using two SLMs. A beam splitter (BS) splits the input laser at 795 nm into a reference beam and a signal beam, and the two SLMs impart correlated phase patterns onto each beam. The phase patterns can be equal-phase or anti-phase to yield phase-insensitive or phase-sensitive cross correlation, respectively. Intensity correlation between the bucket detector output and the pixels of the CCD camera yields the ghost image.

We have made preliminary SLM ghost imaging measurements to demonstrate the feasibility of the two-SLM technique and to show for the first time that ghost imaging can be performed using a classical light source with phase-sensitive cross correlation. The object was a square that was placed with an offset relative to the center of the signal beam (the bright spot in Fig. 9). We used a beam radius of ~200 µm at the SLM and we grouped 2 x 2 pixels of the SLM as one superpixel (30 x 30 µm). The distance between the SLM and the object (or the CCD camera) was ~1 meter and satisfied the far-field requirement for ghost imaging formation for both phase-insensitive and phase-sensitive cross correlations [17]. Figure 9(a) shows the speckle pattern recorded by the CCD camera for one of the equal-phase random patterns, showing clearly that the object cannot be discerned in a single frame. Figure 9(b) shows the ghost image obtained from phase-insensitive cross correlation between the signal and reference beams after averaging for ~2600 frames of equal-phase phase patterns. The center spot indicating the center of the beam and the vertical line passing through it seem to be artifacts of the CCD camera imaging optics, as they also appear in a single frame in Fig. 9(a). For phase-sensitive cross correlation using anti-phase patterns between the signal and reference beams, Fig. 9(c) shows an inverted image of the square, as predicted by theory for far-field phase-sensitive ghost image formation [17]. Note that the two images have similar signal-to-noise ratios and resolutions.

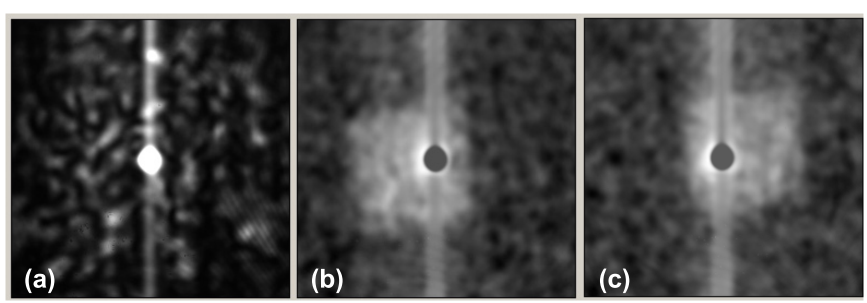

Figure 9. (a) Single frame of speckle pattern recorded by CCD camera, showing no discernable image of the object. (b) Phase-insensitively cross correlated ghost image of the light-grey square that is placed offset from the center of the beam. (c) Phase-sensitively cross correlated ghost image of the same square that is inverted relative to the beam, as predicted by theory for far-field ghost image formation.

<u>Sub-Rayleigh Imaging</u> The Rayleigh diffraction bound sets the minimum separation for two point objects to be distinguishable in a conventional imaging system. Due to diffraction, the image of a

point source through a lens of diameter d and focal length F is an Airy disk with a separation R between the center to the first zero given by $R = 1.22\lambda F/d$. Feature sizes less than R at the image plane cannot be resolved. This is the principle dictating that large-diameter telescopes (larger d) are needed to improve resolution (smaller R).

We have previously proposed an active imaging technique to go beyond the Rayleigh resolution limit by using focused-beam illumination of an object and employing N-photon detection [23]. Consider a point source with an Airy-disk imaged output whose peak has a maximum average detected photon number N_{max}. The N-photon detection strategy sets a detection threshold $N > N_{max}$ such that a measurement of exactly N photons constitutes a value of 1 for a pixel; otherwise, the pixel registers a zero value. For $N > N_{max}$ the pixels near the center of the Airy distribution are more likely to register an N-photon event than those at the wings. Assuming a Poisson distribution of the detected photocounts, the N-photodetection distribution is simply the N-th power of the Airy distribution, hence sharpening the spatial distribution of the image and locating the center of the point-source image more accurately.

The sub-Rayleigh resolution obtained for a point source by N-photon detection can be applied to a spatially-extended object if we illuminate the object point by point and measure the corresponding N-photocount output. The point-like illumination can be realized using a focused laser beam with its beam diameter at the object defining the size of the "point" and hence placing a lower bound on the ultimate resolution of this technique. It should be noted that the usual full-object illumination cannot lead to sub-Rayleigh resolution even if N-photon detection is utilized.

We have recently demonstrated this sub-Rayleigh imaging technique in collaboration with Prof. Franco Zappa and visiting graduate student Fabrizio Guerrieri of Politecnico di Milano and Dr. Simone Tisa of Micro Photon Devices. Our collaborators provided the crucial 32 x 32-pixel single-photon counting array to enable N-photon imaging measurements [24]. Part of a U.S. Air Force resolution target mask was used as the object for imaging, as indicated by the arrow in Fig. 10(a). The imaging apparatus had a small aperture (~2 mm diameter) that served to impose the Rayleigh limit on the image of three pairs of alternately clear and opaque stripes, each of 660 μm width at the image plane. Full-object illumination yielded an image in which the stripes cannot be resolved due to the Rayleigh diffraction limit, estimated to be 1.86 mm, as shown in Fig. 10(b). By focusing the illuminating laser at 532 nm to a 20-μm radius at the object and scanning the beam spot in an arbitrary fashion to cover the spatial extent of the object, we obtained the N-photocount image in Fig. 10(c), showing clearly the three stripes of the mask. The resolution improvement is in good agreement with the theoretical prediction of $(N\text{-}N_{max})^{1/2} = 3$, for $N = 23$ and $N_{max} = 14$. In Fig. 10(c) a few of the pixels had a high number of N-photon events and obscured the clarity of the image. By capping the event occurrence to a maximum of 800 (out of 8000 frames per illumination spot) to make the lower-count pixels more visible, we obtained the 3D intensity profile in Fig. 10(d) that reveals the three stripes very clearly. This new imaging method uses a classical light source, tight focusing on the object, and N-photon detection to yield sub-Rayleigh resolution. It may find useful applications in imaging situations in which precise raster scanning is not possible.

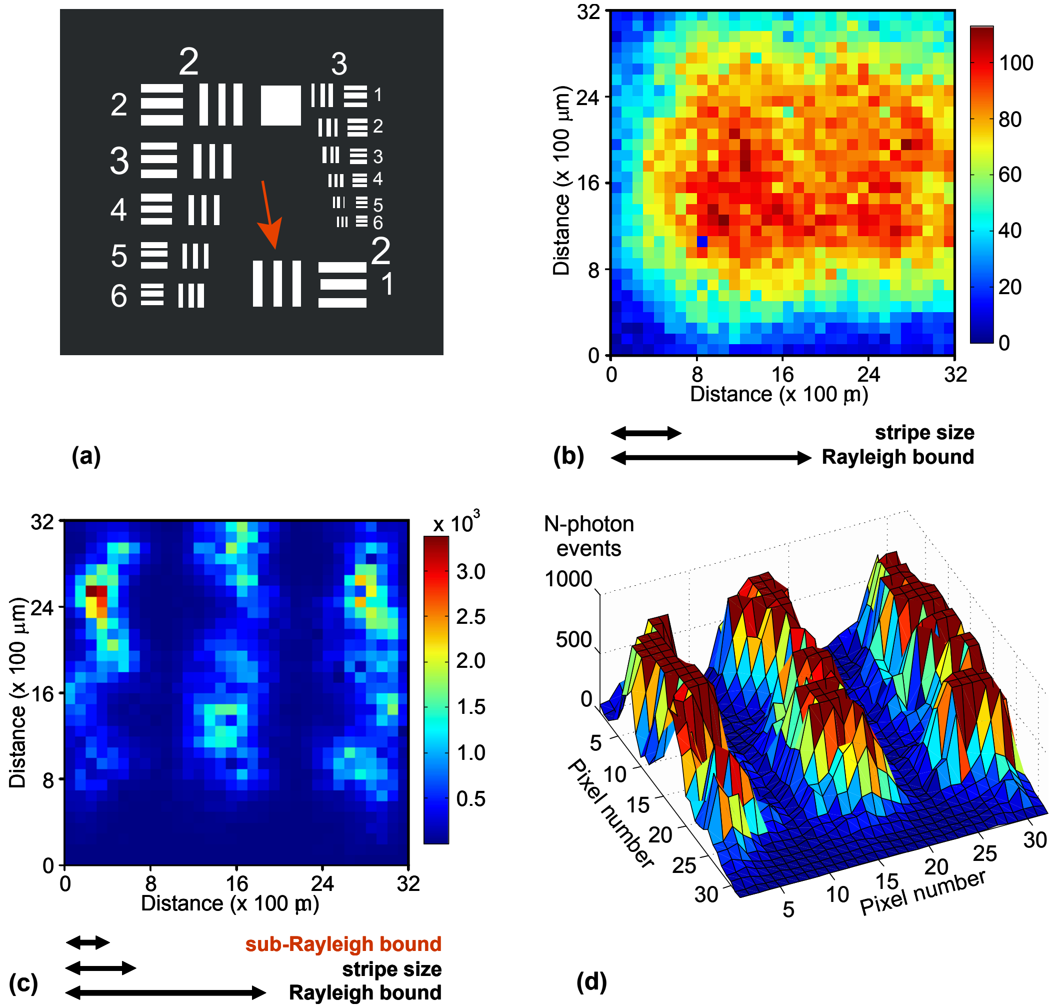

Figure 10. (a) Red arrow indicates part of an US Air Force resolution target to be imaged. (b) Blurred image obtained conventionally using full illumination. (c) Sub-Rayleigh image using focused illumination and N = 23. (d) 3D intensity profile of (c) with the stripes clearly revealed by clipping event counts at 800.

<u>Quantum Illumination</u> Loss and noise can quickly destroy entanglement, so it has commonly been thought that there is little reason to employ entangled light sources in such scenarios. Lloyd [25], however, showed that “quantum illumination” can reap substantial benefits, from the use of entanglement in target detection, despite the presence of loss-destroying loss and noise. In Lloyd’s quantum-illumination paradigm, a photonic source creates d-mode maximally entangled signal and ancilla beams each containing a single photon. The signal beam irradiates a target region containing a very weak thermal-noise bath — with an average of $b << 1$ photons per mode — in which a low-reflectivity object might be embedded. The light received from this region — together with the retained ancilla beam — is then used to decide whether the object is present or absent. Lloyd showed that quantum illumination, with the optimum joint measurement on the received light and the ancilla, achieves a much higher signal-to-background ratio than that realized by optimum quantum reception of light received in response to transmission of a single unentangled photon.

The analysis in [25] was confined, for the most part, to the vacuum plus single-photon manifold, wherein at most one photon arrives at the receiver during the measurement interval regardless of whether the object of interest is absent or present in the target region. We remedied that deficiency by providing a full Gaussian-state treatment of quantum-illumination target detection [26] by employing the exact quantum statistical model for the entangled signal and idler beams obtained from cw SPDC in the absence of pump depletion [1] in conjunction with the standard model for the lossy, bosonic channel [27]. We showed that in a very lossy, very noisy environment, a low-brightness quantum-illumination system enjoys a substantial improvement in the effective signal-to-background ratio — which translates into a very large reduction in the target-detection error probability — in comparison to that achieved by a coherent-state transmitter of the same average photon number. Just as Lloyd found in [25], the SPDC quantum illumination advantage that we have derived accrues despite there being no entanglement between the light that is received from the target region and the retained idler. Quantum illumination is thus the first example of an entanglement-based performance gain, in a full bosonic-channel setting, that survives entanglement-killing loss and noise.

During the past year, we extended our work on quantum illumination in two significant ways. First, we showed that quantum illumination offers a performance advantage in one-versus-two point-target resolution [28] that it similar to what it provides in one-versus-none target detection. Figure 11(a) shows the one-dimensional geometry that we considered. The problem is to determine the minimum angular separation at which we can make a reliable — 0.03 error probability — decision as to whether one or two point objects, which reflect equal power back to the receiver, are present. Figure 11(b) shows that the use of a cw-SPDC quantum illumination system outperforms a coherent-state (laser) system of the same average transmitted power.

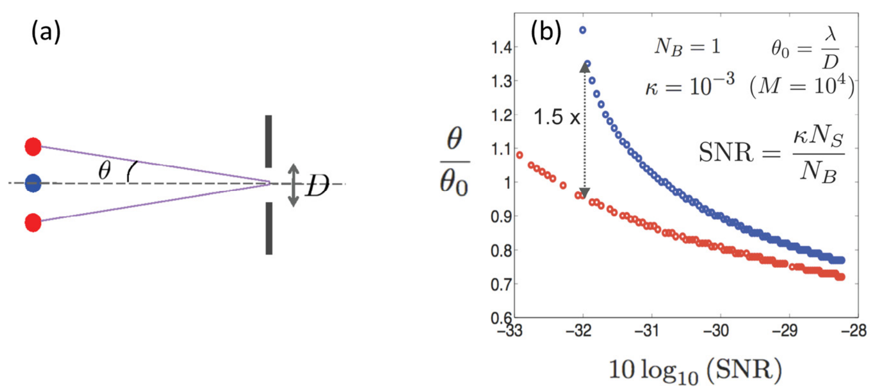

Figure 11. (a) One-dimensional geometry for one-versus-two target resolution problem. Under hypothesis H_1 there is a single on-axis specular point target. Under hypothesis H_2 there are two, identical, in-phase specular point targets symmetrically disposed at angle θ about the axis. A quantum-illumination receiver is employed with a diameter-D entrance pupil. (b) Performance of the quantum-illumination system (red) versus a coherent-state system of the same average transmitted power and wavelength (blue), showing the normalized angle — relative to the diffraction limit λ/D — that each can resolve. N_S is the average signal photon-number per mode that is transmitted; N_B is the average background photon-number per mode that is received; M is the number of temporal modes employed; and κ is the roundtrip transmissivity.

<u>Quantum Illumination-based Secure Communication</u> Our most recent theoretical work on SPDC quantum illumination has been the proposal of a novel two-way secure optical communication protocol that is immune to passive eavesdropping [29]. The basic setup for our analysis is shown in Fig. 12. Alice generates multi-temporal mode entangled signal and idler light beams using a cw SPDC source. She sends the signal to Bob over a lossy channel while retaining the idler. Each T-sec-long transmission (one bit) from Alice comprises $M = WT >> 1$ signal-idler mode pairs, where W is the bandwidth of the signal and idler fields. Each of these modes has a mean photon number $N_S = N_I << 1$. Bob encodes the desired information by modulating the received signal phase using binary phase-shift keying (BPSK). He then amplifies the signal with a phase-insensitive optical amplifier — to compensate for loss and add a significant amount of noise — before sending it back to Alice, again over a lossy channel. Alice makes a joint measurement on

the returned signal (plus noise) and the retained idler to extract Bob's information. We assume that eavesdropper Eve obtains all the photons lost en route from Alice to Bob and from Bob to Alice, and that Eve has access to an optimal quantum receiver while Alice only has access to a receiver we know how to build, viz., the optical parametric amplifier (OPA)-based receiver described in [30]. Alice then enjoys several orders of magnitude better error probability than Eve, as seen in Fig. 13, which plots upper and lower bounds on the error probability of Eve's optimum quantum receiver and upper bounds on the error probability of Alice's optimum quantum receiver — whose implementation is unknown — and her OPA receiver. Alice's performance advantage relative to Eve originates from the stronger-than-classical phase-sensitive cross correlation between the signal and idler created by the SPDC source, which gives her enhanced sensitivity despite the fact that the entanglement between the noisy returned signal and the idler has been destroyed by loss and noise. From Fig. 13 we have that with W = 1 THz and T = 20 ns we can get 50 Mbit/s communication over 50 km of 0.1 dB/km loss fiber (when other losses can be neglected) with Alice's OPA receiver having an error probability of less than 5.1 x 10^{-7} and Eve's optimum quantum receiver having an error probability bounded between 0.28 and 0.46.

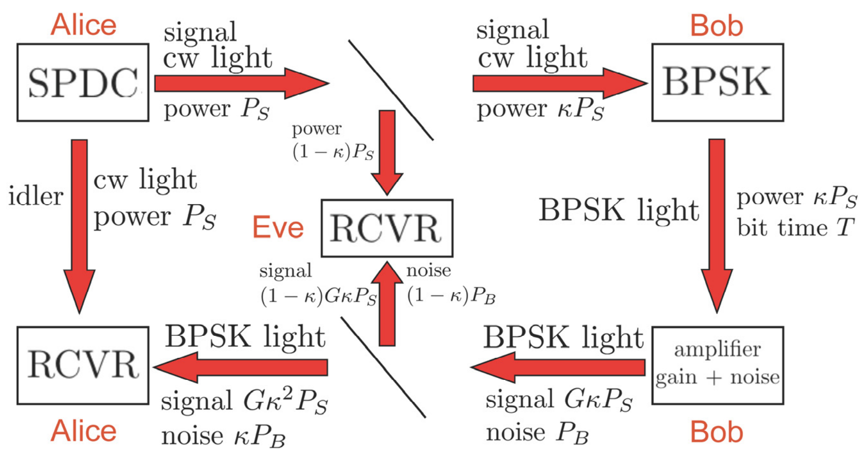

Figure 12. Two-way communication protocol using quantum illumination that is immune to passive eavesdropping.

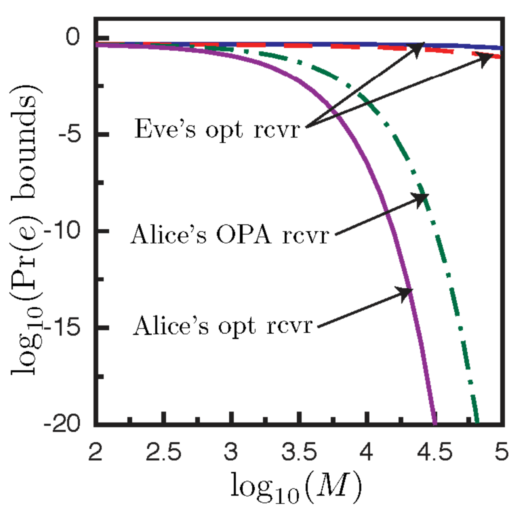

Figure 13. Theoretical performance — error probability bounds versus number of modes employed – for the two-way communication protocol using quantum illumination. The parameters assumed are: N_S = 0.004; κ = 0.1; and $G = N_B = 10^4$.

We are in the process of performing a proof-of-principle experiment of this secure communication protocol. In our fiber-based implementation, shown in Fig. 14, the broadband output from a cw-pumped periodically-poled MgO-doped lithium niobate (PP-MgO:LN) crystal SPDC source was coupled into a single-mode fiber and separated by a coarse wavelength division multiplexer (CWDM) into signal and idler beams centered at 1550 and 1570 nm, respectively. For ~100 mW of pump we measured 180 pW of signal at the CWDM output (bandwidth of ~16 nm). After signal amplification of 40 dB in an erbium-doped fiber amplifier (EDFA) we estimated a signal power of 200 nW plus 1.6 mW of noise at its output. This very significant amount of noise frustrates would-be eavesdroppers who gain very little information without the conjugate idler. Our initial measurements were to test the weakly-pumped OPA receiver in its ability to extract the weak encoded signal. Figure 15 shows the OPA-receiver signal for a square-wave (0–π) input phase modulation at 20 kHz in the (a) time domain and (b) frequency domain. The measured signal strength was ~10x smaller than expected (100x less in signal-to-noise ratio), which was caused by dispersion of the 0.25-ps (16-nm bandwidth) signal pulse through ~70-m of standard fiber and a smaller amount of the idler pulse through a combination of standard and low-dispersion fibers in the idler arm. We verified that no OPA-receiver signal was measurable when the idler light (~100 pW) was blocked, clearly suggesting that the error probability would be high (~0.5) without the idler field. Work is ongoing to: compensate the dispersion with a pair of gratings and hence better recover the dispersion-impaired signal; implement standard communication protocol; and construct an Eve with which to verify the bit error rate disparity between Alice and Eve.

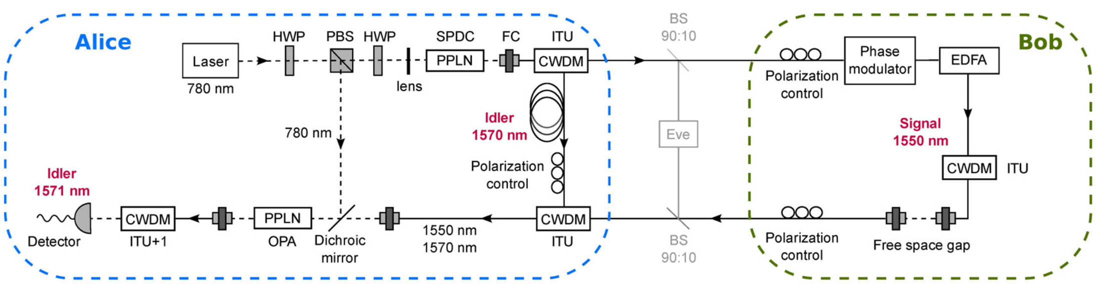

Figure 14. Experimental setup for quantum illumination-based secure communication. The eavesdropping channel, schematically denoted by Eve, is not implemented in the initial experiment.

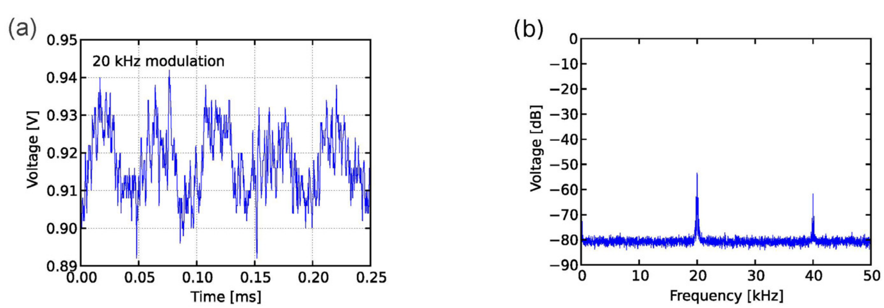

Figure 15. Measured OPA-receiver signal in the (a) time domain, and (b) frequency domain, for a 0–π input square-wave phase modulation at 20 kHz.

<u>Quantum-Enhanced Laser Radar Operation</u> A key feature of a remote sensing system is its ability to obtain detailed spatial information about targets of interest, in both transverse and longitudinal (range) dimensions. High-resolution spatial information is essential for such tasks as target classification, image processing, and tracking of multiple closely-spaced targets. For

modes-range (1–100 km) terrestrial applications under clear-weather conditions laser radar systems offer superior spatial resolution when compared to microwave radars, owing to their use of much shorter wavelengths. When atmospheric turbulence can be neglected, the spatial resolution of such a system is generally limited by the Rayleigh resolution of its receiving optics and the signal-to-noise ratio. We have analyzed two ways in which quantum effects can be used to improve the spatial resolution of a laser radar system that uses conventional, floodlight laser illumination and a soft-aperture entrance pupil in its receiver [31,32], see Fig. 16. Squeezed-vacuum injection (SVI), as proposed in [33], reduces the vacuum noise incurred on the high-spatial-frequency target information that has been attenuated by the soft aperture. SVI requires the use of homodyne detection, so the laser radar receiver is only sensitive to the quadrature in which the noise reduction has occurred. The effectiveness of this noise reduction is, however, severely restricted by inefficiency in that homodyne measurement. Thus, we proposed the use of phase-sensitive amplification (PSA) after the SVI stage and before homodyne detection. PSA enables noise-free amplification of a single field quadrature and hence allows any homodyne inefficiency to be overcome.

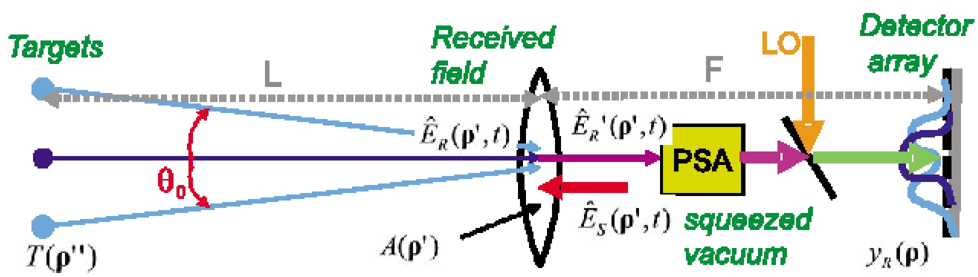

Figure 16. Diagram of quantum-enhanced laser radar receiver. Point targets (one or two) at range *L* are shown at the left. Baseband field operators are shown for the received field and the squeezed-vacuum injected field impinging from the left and the right, respectively, on a soft-aperture pupil function. The combination of these two fields — propagated to an image plane — undergo phase-sensitive amplification and homodyne detection on a continuum array.

Figure 17 shows simulated intensity images for our quantum-enhanced laser radar receiver when the planar target is the US Air Force resolution chart shown in (a) that gives rise to fully-developed speckle. We have assumed a target range L = 1 km, a 15 m x 15 m square target region, 1550 nm laser wavelength, a 4-mm-waist Gaussian soft-aperture pupil inside an 8-mm-diameter hard aperture imaged onto a continuum homodyne-detection array. Figure 17(b) shows the image of the resolution chart after blurring by transmission through the soft aperture. This corresponds to the image in the limit of high SNR and averaging a large number of intensity images with independent speckle. The images in Fig. 17(c)-(f) show detected images averaging over 100 intensity images with independent speckle fluctuations and 25% homodyne efficiency. Figure 17(c) shows the baseline image, i.e., no SVI and no PSA. Figure 17(d) shows the result of adding SVI enhancement with 15 dB of quadrature-noise squeezing to the baseline receiver. Here we see that the low homodyne efficiency has rendered the SVI ineffective. Figure 17(e) shows the result of adding 15 dB of PSA gain to the baseline configuration with no SVI. In this case there is some improvement in the resolution. Figure 17(f) shows the combined value of 15 dB of SVI plus 15 dB of PSA. This figure shows a substantial improvement in image quality over the baseline, SVI-only, and PSA-only images.

In continuing work, we have been relaxing a number of idealizations that were made in [33,34]. Specifically, we have replaced the continuum homodyne array with an array comprised of a finite number of discrete detectors, and we have been working to incorporate more realistic — mode-decomposition — models for the nonlinear optical devices used in the SVI and PSA. So far, our results still indicate that SVI and PSA continue to offer spatial-resolution performance advantages when added to a baseline soft-aperture, homodyne-detection laser radar receiver.

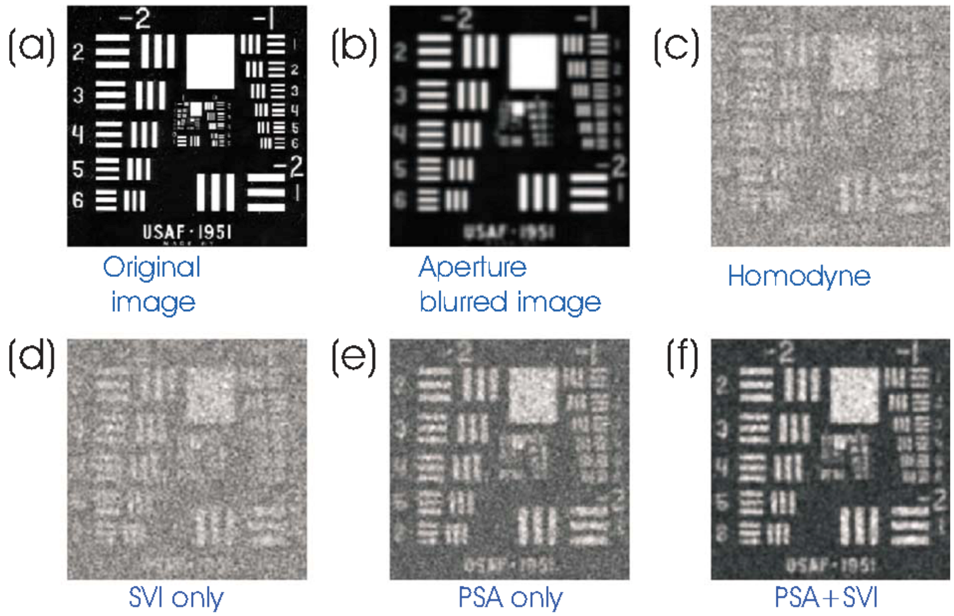

Figure 17. Computer simulated laser radar images. (a) US Air Force resolution chart used as the target. (b) Soft-aperture blurred version of the US Air Force target, i.e., the high SNR image in the absence of speckle. (c) Baseline image of the US Air Force resolution chart obtained with no quantum enhancements. (d) The image obtained when 15 dB of SVI is added to the baseline configuration. (e) The image obtained when 15 dB of PSA is added to the baseline configuration. (f) The image obtained when 15 dB of SVI and 15 dB of PSA is added to the baseline configuration. In (c)-(f) the displayed image is the result of averaging 100 frames with independent speckle and the homodyne array is 25% efficient.

References

1. F. N. C. Wong, J. H. Shapiro, and T. Kim, “Efficient Generation of Polarization-Entangled Photons in a Nonlinear Crystal,” *Laser Phys.* 16, 1517-1524 (2006).

2. T. Zhong, F. N. C. Wong, T. D. Roberts, and P. Battle, "High Performance Photon-Pair Source based on a Fiber-coupled Periodically Poled $KTiOPO_4$ Waveguide," *Opt. Express* 17, 12019-12030 (2009).

3. T. Zhong, X. Hu, F. N. C. Wong, K. K. Berggren, T. D. Roberts, and P. Battle, "High-Quality Fiber-Optic Polarization Entanglement Distribution at 1.3 μm Telecom Wavelength," *Opt. Lett.* 35, 1392-1394 (2010).

4. M. Fiorentino, S. M. Spillane, R. G. Beausoleil, T. D. Roberts, P. Battle, and M. W. Munro, “Spontaneous Parametric Down-Conversion in Periodically Poled KTP Waveguides and Bulk Crystals,” *Opt. Express* 15, 7479-7488 (2007).

5. X. Hu, T. Zhong, J. E. White, E. A. Dauler, F. Najafi, C. H. Herder, F. N. C. Wong, and K. K. Berggren, “Fiber-Coupled Nanowire Photon Counter at 1550 nm with 24% System Detection Efficiency,” *Opt. Lett.* 34, 3607-3609 (2009).

6. J. H. Shapiro and N. C. Wong, “An Ultrabright Narrowband Source of Polarization-Entangled Photon Pairs,” *J. Opt. B: Quantum Semiclass. Opt*. 2, L1-L4 (2000).

7. J. H. Shapiro and K.-X. Sun, "Semiclassical versus Quantum Behavior in Fourth-Order Interference," *J. Opt. Soc. Am. B* 11, 1130-1141 (1994).

8. A. F. Abouraddy, M. B. Nasr, B. E. A. Saleh, A. V. Sergienko, and M. C. Teich, "Quantum Optical Coherence Tomography with Dispersion Cancellation," *Phys. Rev. A* 65 053817 (2002).

9. M. B. Nasr, B. E. A. Saleh, A. V. Sergienko, and M. C. Teich, "Demonstration of Dispersion-Canceled Quantum-Optical Coherence Tomography," *Phys. Rev. Lett*. 91, 083601 (2003).

10. T. B. Pittman, Y. H. Shih, D. V. Strekalov, and A. V. Sergienko, "Optical Imaging by Means of Two-Photon Quantum Entanglement," *Phys. Rev. A* 52, R3429-R3432 (1995).

11. M. D'Angelo, M. V. Chekhova, and Y. Shih, ``Two-Photon Diffraction and Quantum Lithography," *Phys. Rev. Lett*. 87, 013602 (2001).

12. Y. Shih, "Quantum Imaging," *IEEE J. Sel. Top. Quantum Electron*. 13, 1016-1030 (2007).

13. F. Ferri, D. Magatti, A Gatti, M. Bache, E. Brambilla, and L. A. Lugiato, "High Resolution Ghost Image and Ghost Diffraction Experiments with Thermal Light," *Phys. Rev. Lett*. 94, 183602 (2005).

14. G. Scarcelli, V. Berardi, and Y. Shih, "Can Two-Photon Correlation of Chaotic Light Be Considered as Correlation of Intensity Fluctuations?," *Phys. Rev. Lett*. 96, 063602 (2006).

15. R. Meyers, K. Deacon, and Y. Shih, "Ghost-imaging Experiment by Measuring Reflected Photons," *Phys. Rev. A* 77, 041801(R) (2008).

16. B. I. Erkmen and J. H. Shapiro, "Optical Coherence Theory for Phase-Sensitive Light," *Proc. SPIE* 6305, 6305G (2006).

17. B. I. Erkmen and J. H. Shapiro, "Unified Theory of Ghost Imaging with Gaussian-State Light," *Phys. Rev. A* 77, 043809 (2008).

18. B. I. Erkmen and J. H. Shapiro, "Gaussian-State Theory of Two-Photon Imaging," *Phys. Rev. A* 78, 023835 (2008).

19. B. I. Erkmen and J. H. Shapiro, "Signal-to-Noise Ratio of Gaussian-State Ghost Imaging," *Phys. Rev. A* 79 023833 (2009).

20. J. H. Shapiro, "Computational Ghost Imaging," *Phys. Rev. A* 78, 061802(R) (2008).

21. Y Bromberg, O. Katz, and Y. Silberberg, "Ghost Imaging with a Single Detector," *Phys. Rev. A* 79, 053840 (2009).

22. N. D. Hardy and J. H. Shapiro, "Ghost Imaging in Reflection: Resolution, Contrast, and Signal-to-Noise Ratio," Proc. SPIE 7815, 78150P (2010).

23. V. Giovannetti, S. Lloyd, L. Maccone, and J. H. Shapiro, "Sub-Rayleigh-Diffraction-Bound Quantum Imaging," *Phys. Rev. A* 79, 013827 (2009).

24. F. Guerrieri, L. Maccone, F. N. C. Wong, J. H. Shapiro, S. Tisa, and F. Zappa, "Sub-Rayleigh Imaging via *N*-Photon Detection," *Phys. Rev. Lett.* 105, 163602 (2010).

25. S. Lloyd, "Enhanced Sensitivity of Photodetection via Quantum Illumination," *Science* 312, 1463-1465 (2008).

26. S.-H. Tan, B. I. Erkmen, V. Giovannetti, S. Guha, S. Lloyd, L. Maccone, S. Pirandola, and J. H. Shapiro, “Quantum Illumination with Gaussian States,” *Phys. Rev. Lett*. 101, 253601 (2008).

27. V. Giovannetti, S. Guha, S. Lloyd, L. Maccone, J. H. Shapiro, B. J. Yen, and H. P. Yuen, “Classical Capacity of Free-Space Optical Communication,” in *Quantum Information, Statistics, Probability* ed. O. Hirota (Rinton Press, New Jersey, 2004).

28. J. H. Shapiro and S. Guha, “Enhanced Standoff Optical Sensing Resolution Using Quantum Illumination,” *Single Photon Workshop 2009*, Boulder, CO, November 3-6, 2009.

29. J. H. Shapiro, “Defeating Passive Eavesdropping with Quantum Illumination,” *Phys. Rev. A* 80, 022320 (2009).

30. S. Guha and B. I. Erkmen, “Quantum-Illumination Receivers for Target Detection,” *Phys. Rev. A* 80, 052310 (2009).

31. Z. Dutton, J. H. Shapiro, and S. Guha, “LADAR Resolution Improvement using Receivers Enhanced with Squeezed-Vacuum Injection and Phase-Sensitive Amplification,” *J. Opt. Soc. Am. B* 27, A63 (2010).

32. Z. Dutton, J. H. Shapiro, and S. Guha, “LADAR Resolution Improvement using Receivers Enhanced with Squeezed-Vacuum Injection and Phase-Sensitive Amplification: Erratum,” *J. Opt. Soc. Am. B* 27, 2007 (2010).

33. P, Kumar, V. Grigoryan, and M. Vasilyev, “Noise-Free Amplification: Towards Quantum Laser Radar,” *14th Coherent Laser Radar Conference*, Snowmass CO, July 9-13 (2007).

Publications

Journal Articles, Published

X. Hu, T. Zhong, J. E. White, E. A. Dauler, F. Najafi, C. H. Herder, F. N. C. Wong, and K. K. Berggren, “Fiber-Coupled Nanowire Photon Counter at 1550 nm with 24% System Detection Efficiency,” *Opt. Lett.* 34, 3607-3609 (2009).

J. H. Shapiro and S. Lloyd, “Quantum Illumination versus Coherent-State Target Detection,” *New J. Phys*. 11, 063045 (2009).

J. H. Shapiro, “The Quantum Theory of Optical Communications,” *IEEE J. Sel. Topics Quantum Electron*. 15, 1547-1569 (2009).

J. H. Shapiro, “Corrections to ‘The Quantum Theory of Optical Communications’,” *IEEE J. Sel. Topics Quantum Electron.* 16, 698 (2010).

J. H. Shapiro, “Defeating Passive Eavesdropping with Quantum Illumination,” *Phys. Rev. A* 80, 022320 (2009).

Z. Dutton, J. H. Shapiro, and S. Guha, “LADAR Resolution Improvement using Receivers Enhanced with Squeezed-Vacuum Injection and Phase-Sensitive Amplification,” *J. Opt. Soc. Am. B* 27, A63 (2010).

Z. Dutton, J. H. Shapiro, and S. Guha, “LADAR Resolution Improvement using Receivers Enhanced with Squeezed-Vacuum Injection and Phase-Sensitive Amplification: Erratum,” *J. Opt. Soc. Am. B* 27, 2007 (2010).

J. Le Gouët, D. Venkatraman, F. N. C. Wong, and J. H. Shapiro, “Experimental Realization of Phase-Conjugate Optical Coherence Tomography,” *Opt. Lett.* 35, 1001-1003 (2010).

J. H. Shapiro, “Dispersion Cancellation with Phase-Sensitive Gaussian-State Light,” *Phys. Rev. A* 81, 023824 (2010).

T. Zhong, X. Hu, F. N. C. Wong, K. K. Berggren, T. D. Roberts, and P. Battle, “High-Quality Fiber-Optic Polarization Entanglement Distribution at 1.3 μm Telecom Wavelength,” *Opt. Lett.* 35, 1392-1394 (2010).

F. Guerrieri, L. Maccone, F. N. C. Wong, J. H. Shapiro, S. Tisa, and F. Zappa, “Sub-Rayleigh Imaging via *N*-Photon Detection,” *Phys. Rev. Lett.* 105, 163602 (2010).

Meeting Papers, Published

J. H. Shapiro, “Defeating Passive Eavesdropping with Quantum Illumination,” *Frontiers in Optics Meeting*, Rochester, NY, October 11-15, 2009.

X. Hu, T. Zhong, F. Najafi, F. Marcili, C. Herder, F. N. C. Wong, E. A. Dauler, and K. K. Berggren, “Efficiently Coupling Light to Superconducting Nanowire Single-Photon Detectors,” *Single Photon Workshop 2009*, Boulder, CO, November 3-6, 2009.

F. N. C. Wong, “Generation of Single Spatiotemporal Mode Photons,” *Single Photon Workshop 2009*, Boulder, CO, November 3-6, 2009.

T. Zhong, X. Hu, F. N. C. Wong, C. Herder, F. Najafi, K. K. Berggren, T. D. Roberts, and P. Battle, “High Quality Photonic Polarization Entanglement Distribution at 1.3-μm Telecom Wavelength,” *Single Photon Workshop 2009*, Boulder, CO, November 3-6, 2009.

J. H. Shapiro and S. Guha, “Enhanced Standoff Optical Sensing Resolution Using Quantum Illumination,” *Single Photon Workshop 2009*, Boulder, CO, November 3-6, 2009.

J. Le Gouët, D. Venkatraman, F. N. C. Wong, and J. H. Shapiro, “Experimental Realization of Phase-Conjugate Optical Coherence Tomography,” *18th International Laser Physics Workshop*, Barcelona, Spain, July 13-17, 2009.

J. H. Shapiro, Z. Dutton, and S. Guha, “Improving Laser Radar Spatial Resolution by Squeezed-Vacuum Injection,” *18th International Laser Physics Workshop*, Barcelona, Spain, July 13-17, 2009.

R. García-Patrón, F. N. C. Wong, and J. H. Shapiro, “Optimal Individual Attack on BB84 Quantum Key Distribution using Single-Photon Two-Qubit Quantum Logic,” *SPIE Proceedings on Quantum Information and Computation VIII*, Orlando, FL, April 5-9, 2010.

J. H. Shapiro, “Dispersion Cancellation with Phase-Sensitive Gaussian-State Light,” *Digest of Quantum Electronics and Laser Science Conference*, San Jose, CA, May 16-21, 2010.

F. Guerrieri, L. Maccone, F. N. C. Wong, J. H. Shapiro, S. Tisa, and F. Zappa, “Sub-Rayleigh Imaging via N-Photon Detection,” *Digest of Quantum Electronics and Laser Science Conference*, San Jose, CA, May 16-21, 2010.

A. H. Nejadmalayeri, J. A. Cox, F. N. C. Wong, T. D. Roberts, P. Battle, and Franz X. Kärtner, “Phase Noise Measurement of Mode Locked Lasers using Guided Wave PPKTP Balanced Cross

Correlators," *Digest of Conference on Lasers and Electro-Optics*, San Jose, CA, May 16-21, 2010.

N. D. Hardy and J. H. Shapiro, "Ghost Imaging in Reflection: Resolution, Contrast, and Signal-to-Noise Ratio," *SPIE Proceedings on Quantum Communications and Quantum Imaging VIII*, San Diego, CA, August 4-5, 2010.

Theses

B. Mookerji, "Generation of Fiber-Coupled, Nondegenerate, Polarization-Entangled Photons for Quantum Communication," S.B. thesis, Department of Physics, MIT 2009.

T. Zhong, "High Performance Photon-Pair Source based on a Fiber-Coupled Periodically Poled $KTiOPO_4$ Waveguide," S.M. thesis, Department of Electrical Engineering and Computer Science, MIT 2009.